International Journal of Agriculture, Environment and Food Sciences
e-ISSN : 2618-5946
www.jaefs.com
Research Article
Int J Agric Environ Food Sci 6 (3): 480-493 (2022)

Structural changes in fasted state dietary mixed micelles upon solubilization of beta-carotene

Beste Bayramoğlu[1,*]

[1]Food Engineering Department, Faculty of Engineering, Izmir Institute of Technology, Izmir, Türkiye

[*]Corresponding Author: bestebayramoglu@iyte.edu.tr

Citation
Bayramoglu, B. (2022). Structural changes in fasted state dietary mixed micelles upon solubilization of beta-carotene. International Journal of Agriculture, Environment and Food Sciences, 6 (3), 480-493
Doi: https://doi.org/10.31015/jaefs.2022.3.18

Received: 11 August 2022
Accepted: 16 September 2022
Published Online: 20 September 2022

Year: 2022
Volume: 6
Issue: 3 (September)
Pages: 480-493

Available online
http://www.jaefs.com
https://dergipark.org.tr/jaefs

Abstract

It was aimed to investigate the structural changes taking place in duodenal mixed micelles (MM) at fasted state with the incorporation of fatty acids (FA) and the morphological transformations in these MMs upon solubilization of β-carotene (BCR) through coarse-grained (CG) molecular dynamics (MD) simulations. All simulations were performed with GROMACS 2019 simulation package using the Martini force field. Lauric acid (LA), stearic acid (SA) and linoleic acid (LNA) were used to explore the effects of FA chain length and unsaturation. Micelle swelling was observed with the incorporation of all FAs. The increase in size was in line with increasing FA chain length and unsaturation. MMs incorporating LA and SA were ellipsoidal in shape, while polyunsaturated LNA resulted in a worm-like MM. Upon solubilization of BCRs, swelling was observed only in the MMs with long-chain SA and LNA. No micelle growth was observed in the plain and LA MMs despite their smaller sizes. This was attributed to their low-density hydrophobic cores, which allowed a condensation effect induced by the interactions between BCRs and POPC tails. It is inferred that when the micelle is large enough to solubilize BCRs, whether or not swelling will take place depends on the core density. The increase in micelle size was very small in the MM incorporating LNA compared to that in the MM with SA, which was accompanied by an elliptical-to-cylindrical shape transformation. This was due to the fluid nature of the worm-like LNA micelle, which readily allowed the solubilization of 3 BCRs within its core. By resolving the internal structures of BCR incorporated MMs, this study gives valuable insight into the effects of FA chain length and unsaturation on the solubilization behavior of dietary MMs. The results are expected to give direction to the development of rational design strategies for effective BCR delivery systems.

Keywords

Molecular dynamics simulation, β-carotene, Dietary mixed micelle, Bioaccessibility, Nutraceutical delivery system

Introduction

Carotenoids are natural lipid-soluble color pigments found mainly in fruits and green leafy vegetables. They have many health-promoting effects and are known to have an important role in reducing the risk of cardiovascular diseases, cancers, and blurred vision. (Yao et al., 2019). β-carotene is one of the best-known carotenoids possessing the highest provitamin A activity (Qian et al., 2012). It is widely found in nature and used as a colorant and nutritional supplement in foods (Tunçer, 2018). However, β-carotene bioavailability is very low, owing to its highly lipophilic nature, which limits its solubilization in the aqueous intestinal lumen. Some strategies have been proposed to enhance the oral bioavailability of β-carotene. One approach involves development of food-grade delivery systems with specific characteristics that will allow the formation of colloidal structures in the intestinal fluids in which β-carotene is effectively solubilized (Tunçer and Bayramoğlu, 2022). This strategy clearly targets improving β-carotene bioaccessibility; i.e., the fraction of the orally administered bioactive compound solubilized within the supramolecular assemblies of small intestine. As only the amount solubilized in these assemblies is considered to be available for absorption by epithelial cells (Yuan et al., 2018), this step plays a key role in the enhancement of β-

carotene bioavailability.

Delivery systems are lipid-based formulations consisting of colloidal structures of various sizes and morphologies, which encapsulate and protect bioactive components (Tunçer and Bayramoğlu, 2022). Upon digestion of the constituents within the gastro-intestinal (GI) tract, digestion products including fatty acids (FA) and the bioactive molecules are incorporated with bile salts (BS) and phospholipids (PL) into dietary mixed micelles (MM) in the duodenum (Qian et al., 2012). This implies that the improvement in the bioaccessibility of the bio-actives depends on the nature of the MMs formed (Yao et al., 2019). The formulations should be prepared based on the knowledge about how the constituents of the delivery system affect the structural characteristics of MMs formed in duodenum. Although it is well known that fed state (postprandial) duodenal conditions increase the bioavailability of various lipophilic nutrients, it is usually the fasted state conditions, which is of primary interest to the formulators as the absorption environment is more challenging in the latter. Therefore, the aim is to develop optimal delivery systems that would give, upon their digestion in the GI tract, predictable and favorable assembly structures in the duodenum at fasted state and yield an equivalent bioavailability for the bioactive compound compared to fed state (Birru et al., 2014). Depending on the total lipids concentration in the environment, coexistence of MMs with uni- or multi-lamellar vesicles has been reported at fasted state (El Aoud et al., 2021). In order to develop effective delivery systems for β-carotene, a deep understanding of how this molecule is solubilized within such structures is needed.

It is known that lipid digestion products improve carotenoid micellarization. The FA chain length and unsaturation are the two important modulating factors. Many researchers have shown that long-chain FAs function better in terms of improving the bioaccessibility of β-carotene compared to medium-chain FAs (Huo et al., 2007; Nagao et al., 2013; Qian et al., 2012; Yao et al., 2019; Yuan et al., 2018), which is mainly attributed to the increased hydrophobic core volumes of MMs. Mashurabad et al. have reported that dietary fat rich in unsaturated FAs yielded significantly better β-carotene micellarization compared to saturated FAs (Mashurabad et al., 2017). On the other hand, Huo et al. determined the degree of unsaturation was ineffective in β-carotene bioaccessibility (Huo et al., 2007). Nagao et al. reported increased bioaccessibility of β-carotene with unsaturated FAs although the performance of polyunsaturated FAs was found to be lower compared to monounsaturated FAs (Nagao et al., 2013). As a matter of fact, there are many more studies addressing β-carotene bioaccessibility in the literature. However, they mostly lack an appropriate structural characterization of the MMs solubilizing these molecules. Accordingly, very little is known about the structural changes taking place in the MMs upon solubilization of carotenoids as well as the details of the internal morphology and the interactions between the constituent molecules. This kind of knowledge is believed to be crucial in giving direction to rational design strategies for the development of effective carotenoid delivery systems. This study aims to contribute to filling this gap through CG MD simulations on the solubilization of β-carotene within duodenal MMs at fasted state. Recently, the self-assembly of bile lipids in mimicking duodenal environments both at fasted and fed state were simulated and the resulting colloidal assemblies were structurally characterized by an MD study in our group (Tuncer and Bayramoglu, 2019). However, due to the use of limited system sizes imposed by available computational sources, only the lower-size micelle fraction of the whole duodenal colloidal landscape of fasted state was reproduced. Unfortunately, it is computationally quite demanding to reproduce the true thermodynamic equilibrium phase of duodenum at fasted state (a mixture of several MMs and vesicles) even with CG models. Therefore, this work was restricted to the analysis of a single representative MM. A different approach has been adopted here in order to obtain the representative fasted state MM (composed of only BSs and PLs) with the desired size and shape properties. Next, solubilization of different types of FAs within the representative MM has been explored with a focus on the effects of FA chain length and unsaturation on the micelle morphology. It is followed by a detailed characterization of the structural changes taking place upon solubilization of β-carotene molecules in these micelles. To the best of our knowledge, this is the first study that demonstrates the accompanying structural transformations in MMs with solubilization of BCRs and resolves the internal morphology at molecular level. The results obtained in this work will contribute to the knowledge in the field and are expected to facilitate the development of effective β-carotene delivery systems.

Computational Methods

Details of the Systems Studied

Sodium cholate (CHOA) and POPC were used as the model BS and PL, respectively. The presence of cholesterol in the duodenal MMs was ignored as it is diluted in the small intestine (Wilson and Rudel, 1994), and has no significant effect on the micelle structure and dynamics (Marrink, 2004; Matsuoka et al., 2004; Suys et al., 2017; Tunçer and Bayramoğlu, 2022). In order to investigate the effects of FA chain length and unsaturation on the micelle morphologies, three different FAs, namely, lauric acid (12:0), (LA), stearic acid (18:0) (SA) and linoleic acid (18:2) (LNA) were studied. All CHOAs were used in their deprotonated forms as the pKa of CHOA is ~5.5 (Bustos et al., 2011), which is smaller than the duodenal pH at fasted state (~7). The possibility of varying ionization degree of FAs with respect to local environment was not taken into account to maintain the simplicity of the study (Tunçer and Bayramoğlu, 2022), thus all FAs were used in their negatively charged forms. All the simulation boxes were solvated with the required amounts of water molecules, while the physiological NaCl concentration (150 mM) was maintained by addition of appropriate numbers of Na+ and Cl- ions. Additional Na+ ions were supplemented to neutralize the systems. The simulation box size was 13 nm x 13 nm x 13 nm in all systems, which was confirmed to be large enough to avoid finite size effects by parallel simulations. The compositions of all systems are given in Table 1. For the simulations involving solubilization of BCR in the representative micelles, 3 BCR molecules were used in each system since it was also aimed to examine the interactions between BCRs in a micelle. Although this results in a very high BCR-to-FA ratio (~5 % w/w) when

compared to the bulk solubility of BCR in triglycerides (0.11-0.14% w/w) (Wright et al., 2008), the system sizes were strictly limited by the overwhelming computational costs. As a matter of fact, considering the local variations *in vivo* due to the dynamic nature of lipid lipolysis concurrently occurring with micellization, it is not unlikely that more than 3 BCRs can be solubilized within MMs that are as large as obtained in this work.

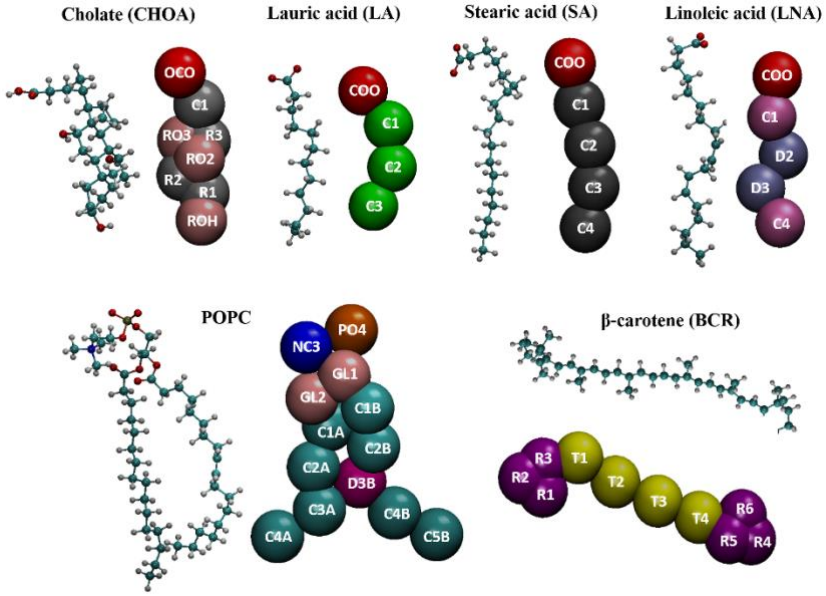

Figure 1. Atomistic and CG structures of the molecules used in the study. In the atomistic models, the oxygen, carbon, nitrogen, phosphorus and hydrogen are represented by red, cyan, navy, tan and white balls, respectively. In the CG models, the names of the interaction sites on each molecule are given.

The Martini force field (Marrink et al., 2007; Marrink and Tieleman, 2013) was used in the simulations. Four heavy atoms together with the associated hydrogens are grouped into a single Martini CG bead in Martini model. For ring structures, 2- or 3-to-1 mapping is applied for higher resolution. Four real water molecules are grouped into a single CG water bead, and the CG beads of single atom ions are represented with their first hydration shell (Tunçer, 2018). The configuration and topology files of the constituent molecules except for NA were supplied from the Martini website (Martini General Purpose Coarse-Grained Force Field, 2022). The parameters of hydrocarbon tails of 1,2-dilinoleoyl-sn-glycero-3-phosphocholine (DUPC) were used to construct the model for NA tail (de Jong et al., 2015; Tunçer and Bayramoğlu, 2022). The head group parameters of SA were used for the NA head group. Fig. 1 demonstrates the molecular structures and mapping between the atomistic and CG atoms.

Table 1. Number of coarse-grained molecules/ions in the simulation boxes (13 x 13 x 13 nm^3) of systems studied in this work. CHOA: cholate, FA: Fatty acid, BCR: beta-carotene, LA: Lauric acid, SA: Stearic acid, LNA: Linoleic acid.

System	CHOA:POPC:FA:BCR	Water	Na^+:Cl^-
Fa	110:66:-:-	16536	308:198
Fa-BCR	110:66:-:3	16439	308:198
Fa-LA	110:66:110:-	15932	418:198
Fa-SA	110:66:110:-	15828	418:198
Fa-LNA	110:66:110:-	15884	418:198
Fa-LA-BCR	95:66:79:3	16140	372:198
Fa-SA-BCR	110:66:110:3	15821	418:198
Fa-LNA-BCR	110:66:110:3	15782	418:198

System Setup and Simulation Procedure

Several experimental studies have shown that the average hydrodynamic radius (R_h) of duodenal plain MMs (composed of only BSs and PLs) at fasted state concentrations (5 mM BSs+1.25 mM PLs) is around 3.5 nm (Clulow et al., 2017; Khoshakhlagh et al., 2014; Kossena et al., 2003; Mazer et al., 1980; Schurtenberger et al., 1985). As it would be computationally too expensive to simulate the duodenal medium composed of several micelles at such low BL concentrations even when using Martini model, the approach of Marrink and Mark (Marrink and Mark, 2002) was followed to construct a single representative fasted state plain MM. It is expected that the duodenal micelles are spheroidal in shape at a PL:BS ratio of 1:4 (Clulow et al., 2017; Hjelm et al., 1990). Based on the information that the ratio of the radius

of gyration (R_g) of a solid sphere to its R_h is 0.77 (Tande et al., 2001), the R_g of the representative plain MM was predicted to be ~2.7 nm. The initial configuration of the pre-assembled spherical POPC micelle was generated using CHARMM-GUI micelle builder tool (Cheng et al., 2013). Appropriate amounts of CHOA molecules were placed randomly around this micelle in the simulation box, which was later solvated with water. Required number of Na+ and Cl- ions were added to achieve a NaCl concentration of 150 mM and to neutralize the system. Softcore minimization with flexible waters and position restraints ($k_{x,y,z}$ = 1000 kJ/mol.nm^2) on POPC's PO4 beads was applied using the steepest descent algorithm with a step size of 0.01 nm. It was followed by a series of NVT equilibration steps at 310 K, each lasting for 2 ns (dt = 40 fs), using position restraints on PO4 with decreasing force constants (200-20 kJ/mol.nm^2). Finally, the system was equilibrated further at 1 bar and 310 K through a 2 ns NPT run (dt = 40 fs) using Berendsen temperature and pressure coupling schemes (tau_t = 1 ps, tau_p = 3 ps). Parallel simulations have been conducted to determine the appropriate total number of BLs, the POPC:CHOA ratio in the simulation box and the box size. The production run (5 μs) was started at NPT ensemble with a time step of 20 fs on the system of choice, which resulted in a spheroidal MM composed of 66 POPC and 86 CHOA molecules with an R_g of 2.7 nm.

For the setup of the Fa-BCR and Fa-LA/SA/LNA systems, the plain MM mentioned above was extracted to separate simulation boxes of same length (13 nm), and 24 CHOA molecules were added randomly around the micelle to maintain a constant inter-micellar free BS concentration. After the random placement of 3 BCR or 110 FA molecules in the boxes, similar steps were followed to add water and ions to the systems. The choice of CHOA:FA ratio was based on previous experimental studies (Fatouros et al., 2009; Phan et al., 2015). Similarly, the construction of the initial configurations for the 3 remaining systems (Fa-LA/SA/LNA-BCR) started with the extraction of the corresponding representative micelles from systems Fa-LA/SA/LNA into separate simulation boxes of same length. Free CHOAs, 3 BCR molecules, water and ions were added following the same procedures. Once the initial configurations were constructed, energy minimization was applied using steepest descent method with a step size of 0.01 nm without any position restraints. It was followed by equilibration runs of 2-5 ns at constant NPT (1 bar, 310 K) with a time step of 40 fs. The production runs (dt=20 fs) at NPT ensemble lasted for 5 μs for all the systems involving BCR, and 10 μs for the remaining systems.

All simulations were carried out using GROMACS simulation 2019 package (Abraham et al., 2015; Van Der Spoel et al., 2005). All the systems were simulated in cubic simulation boxes with periodic boundary conditions using standard Martini parameters (Marrink et al., 2007). Non-bonded interactions were treated with a Lennard Jones 12–6 potential using a smooth shift to zero between 0.9 and 1.2 nm. Electrostatic interactions were defined by Coulomb potential with a relative permittivity of 15 and a shift function from 0 to 1.2 nm. Lincs algorithm (Hess et al., 1997) was used to constrain CHOA bond lengths when present. The initial velocities were assigned with a Maxwell-Boltzmann distribution at 310 K. Temperature and pressure were coupled at 310 K and 1 bar using the Berendsen thermostat and barostat (Berendsen et al., 1984) with a time constant of 1 ps, respectively. The neighbor list was updated every 10 steps.

Analysis Methods

An appropriate clustering criterion (cutoff value) needs to be chosen to initiate the analyses on micelles. In this study, a cutoff value of 0.6 nm was used based on previous experience (Tuncer and Bayramoglu, 2019; Tunçer and Bayramoğlu, 2022). This choice assures that the molecules are considered to be in the same cluster if the distance between their closest CG interaction sites is smaller than 0.6 nm. To monitor the convergence points of simulations, time dependent number of free CHOA molecules and weight-averaged aggregation numbers (N_w) were calculated using this cutoff value according to Sayyed-Ahmad et al (Sayyed-Ahmad et al., 2010). Due to the dynamic exchange of CHOAs between the micelle and the aqueous environment, steady state micelle aggregation numbers showed broad distributions. The detailed structural analyses were performed on the micelle that remained intact for the longest time during the production runs for each system. The choice was based on the time dependent cumulative probability distributions of micelle aggregation numbers, which were calculated in a block-averaged fashion over 1 μs periods. The radii of gyration (R_g), the ratios of the principle moments of inertia and the solvent accessible surface area (SASA) were calculated to analyze the global structures. An imaginary solvent probe of 0.56 nm in radius was used to mimic one Martini water bead, which represents four atomistic water molecules, to calculate SASA. The local structures were investigated through the radial density distributions (RDDs), as well as the average angles between selected vectors in a molecule (Type II) and with respect to the local micelle normal (Type I) (only for spheroidal micelles). The last two were calculated to analyze the molecular conformations and surface orientations of the constituent molecules with respect to the micelle radial vector, respectively. The systems and the trajectories were visualized by Visual Molecular Dynamics (VMD, version 1.9.2) (Humphrey et al., 1996).

Results and Discussion

Structural Properties of the Representative Duodenal Cholate-POPC Mixed Micelle at Fasted State

The final frame corresponding to the simulations of the system named 'Fa' is given in Fig.2a. The time dependent number of free CHOAs and N_w data (not shown) indicated that the simulations for the representative plain MM at fasted state converged after 1.5-2 μs. Therefore, the cumulative probability distribution of micelle aggregation number analysis was made over the last 3 μs of the production runs (Fig.3a). The broadness of the distribution is a result of the dynamic exchange of CHOAs between the micelle and the aqueous environment. The results showed that the most stable micelle was composed of 152 members (66 POPC and 86 CHOA residues). The structural properties of the representative fasted state plain micelle are given in Table 2. The radius of gyration of the micelle was found as 2.708 nm. The ratios of three principal moments of inertia (I1/I2 and I2/I3) were calculated (where $I1 \leq I2 \leq I3$) to characterize the shape of micelle. The ratios, I1/I2 and I2/I3, describe the micelle

shapes; i.e., for spherical micelles, I1≈I2≈I3 and I1/I2≈I2/I3≈1; for disc-like micelles, I1≈I2 « I3, and I1/I2≈1 and I2/I3≈0; for rod-like micelles, I1 « I2≈I3, I1/I2≈0 and I2/I3≈1 (Tuncer and Bayramoglu, 2019). Based on the results, it is clear that the representative fasted state plain micelle is slightly ellipsoidal in shape. The findings are in agreement with the literature. For instance, Clulow et al. characterized the nanoaggregates in simulated intestinal fluids by means of small angle x-ray scattering (SAXS) and dynamic light scattering (DLS), cryogenic transmission electron microscopy (cryo-TEM) measurements and MD simulations (Clulow et al., 2017). They determined that the R_g of MMs composed of sodium taurodeoxycholate (TDC) and DOPC at fasted state ranged between 2.6 and 2.8 nm, while the corresponding R_h values ranged in 2.7-3.3 nm. The shapes of the micelles were found as oblate ellipsoids. MD simulations also yielded ellipsoidal MMs with shape factors (the ratio of max and min R_g tensors) ranging in 1.1-1.6. Kossena et al. reported a R_h value of 3.5 nm measured by photon correlation spectroscopy for fasted state MMs composed of TDC and purified egg yolk lecithin (Kossena et al., 2003). Others also reported similar micelle sizes determined experimentally (Fatouros et al., 2007; Mazer et al., 1980; Schurtenberger et al., 1985). Furthermore, Parrow et al. studied the inter-individual variability of human intestinal fluids at fasted state by performing CG MD simulations of model systems mimicking the aspirated duodenal samples from healthy volunteers. They found that the micelle diameters ranged from 2.3 to 7.3 nm, and the shape factors were in the 1.2-1.9 interval indicating ellipsoidal micelles (Parrow et al., 2020).

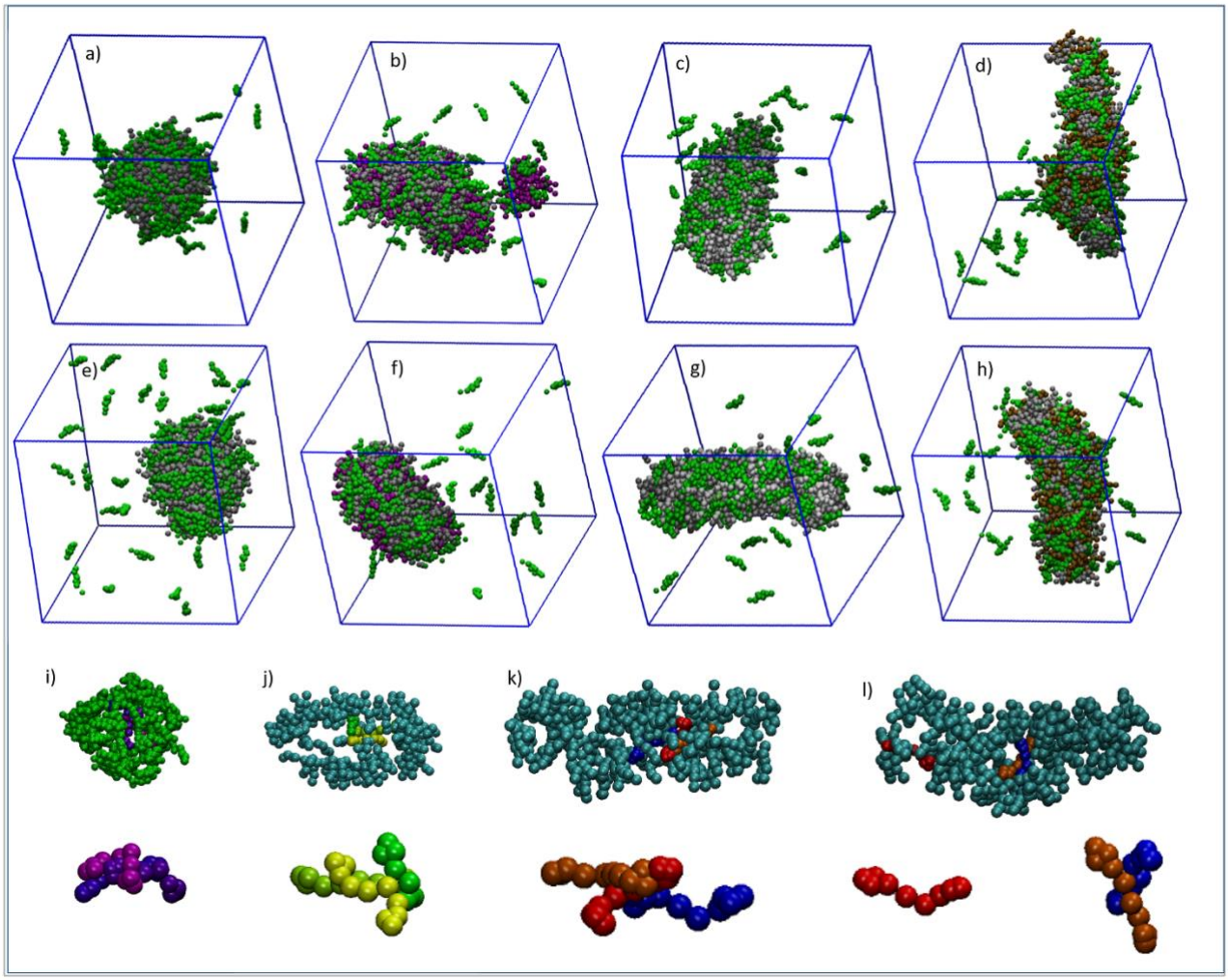

Figure 2. Snapshots from the final frames of systems named in Table 1 as (a) Fa, (b) Fa-LA, (c) Fa-SA, (d) Fa-LNA, (e) Fa-BCR, (f) Fa-LA-BCR, (g) Fa-SA-BCR, (h) Fa-LNA-BCR. For visual clarity, ions and water molecules are not shown. CHOAs, POPCs, LAs, SAs and LNAs are represented by green, grey, purple, white and brown, respectively. Snapshots are given from the representative (i) BCR, (j) LA-BCR, (k) SA-BCR, (l) LNA-BCR micelles and exemplary conformations of BCRs within the micelles. Individual BCR molecules are shown in different colors. Only CHOAs (green) and BCRs are shown in (i), FAs (cyan) and BCRs in (j-l) for visual clarity. The images are not-to-scale.

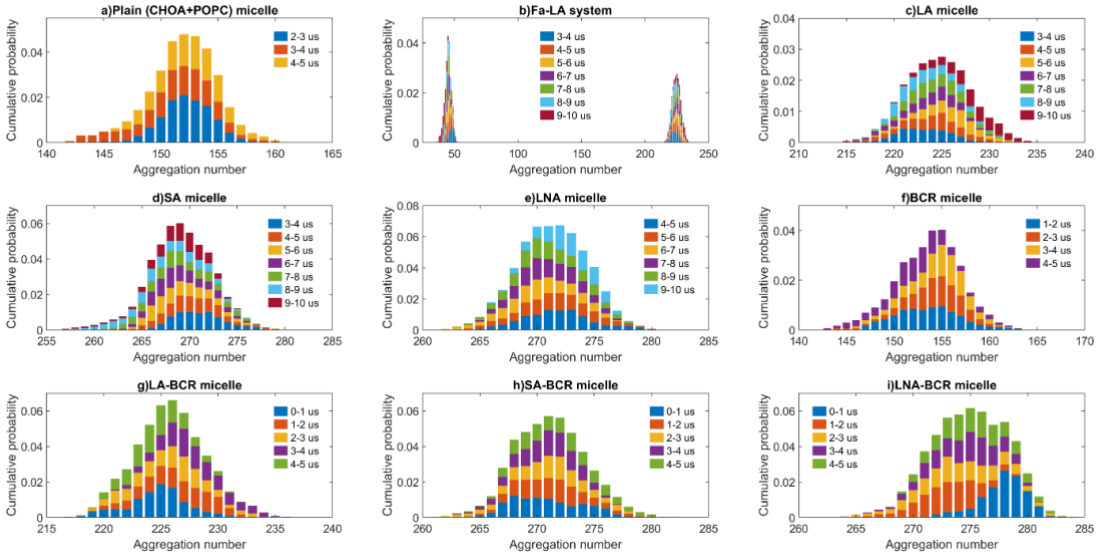

Figure 3. The cumulative probability distributions of micelle aggregation numbers after the convergence point of simulations as a function of time (block-averaged over 1 μs intervals) for the (a) plain (CHOA+POPC) MM, (b) fasted LA system, (c) zoomed-in view of the distribution belonging to the large LA MM shown in (b), (d) SA MM, (e) LNA MM, (f) BCR MM, (g) LA-BCR MM, (h) SA-BCR MM, and (i) LNA-BCR MM.

Table 2. Structural properties of equilibrium micelles.

Micelle aggregation number and composition (CHOA:POPC:FA: BCR)	R_g (nm)	I_1/I_2	I_2/I_3	Total SASA (nm^2)	POPC-oleoyl tail length** (nm)	POPC-palmitoyl tail length** (nm)	FA length **(nm)	BCR length **(nm)
Plain 152 (86:66:-:-) (57%:43%:-:-)*	2.708±0.041	0.742±0.113	0.857±0.059	265.609±8.391	1.437±0.199	1.188±0.129	-	-
BCR 155 (86:66:-:3) (55%:43%:-:1.9%)*	2.673±0.029	0.807±0.084	0.889±0.051	265.528±8.340	1.436±0.198	1.188±0.128	-	2.182± 0.367
LA 225 (80:66:79:-) (36%:29%:35%:-)*	3.264±0.111	0.390±0.089	0.936±0.044	319.414±8.940	1.442±0.197	1.196±0.127	1.210±0.120	-
SA 269 (93:66:110:-) (35%:25%:41%:-)*	3.685±0.146	0.316±0.074	0.935±0.042	364.241±1.142	1.446±0.197	1.197±0.128	1.556±0.164	-
LNA 272 (96:66:110:-) (35%:24%:40%:-)*	4.425±0.345	0.184±0.031	0.969±0.016	344.601±9.302	1.438±0.198	1.196±0.128	1.335±0.236	-
LA-BCR 226 (78:66:79:3) (35%:29%:35%:1.3%)*	3.102±0.094	0.527±0.134	0.885±0.068	311.982±9.064	1.443±0.196	1.196±0.127	1.209±0.119	2.202± 0.347
SA-BCR 271 (92:66:110:3) (34%:24%:41%:1.1%)*	4.395±0.346	0.172±0.029	0.979±0.011	330.665±8.549	1.436±0.198	1.193±0.128	1.554±0.165	2.186± 0.357
LNA-BCR 275 (96:66:110:3) (35%:24%:40%:1.1%)*	4.437±0.350	0.183±0.031	0.972±0.015	345.238±9.059	1.441±0.197	1.197±0.127	1.336±0.237	2.153± 0.371

*Percentage of constituent molecules in the micelles

** Tail/molecule lengths were measured as the average distance between the C1B-C5B, C1A-C4A, COO-C3/C4, R2-R6 beads of POPC-oleoyl tails, POPC-palmitoyl tails, FAs, and BCRs, respectively.

In order to examine the micelle interior structure and the distribution of ions and water around the micelle, radial density distributions (RDDs) of the selected moieties of the constituent molecules with respect to the micelle center of mass (com) were calculated. The corresponding graphs for the plain MM are given in Fig.4(a-b). The reader should refer to Fig.1 for the interpretation of the CG bead names used in the graphs. Fig.4a gives a general idea about the arrangement of molecular groups inside and of ions/waters around the micelles, while Fig.4b provides a closer look at the interfacial region. As expected, the micelle core is occupied solely by POPC tails, and the CHOAs are positioned at the surface. This is in perfect agreement with the results of Clulow et al., who showed that a core-shell ellipsoidal model best fitted the SAXS profiles of fasted state MMs, which was further confirmed by MD simulations revealing that the cores were rich in alkyl-chains while the shells were rich in BSs (Clulow et al., 2017). Water, which totally solvates the charged head groups of POPCs (PO4- and NC3+) and CHOAs (OCO-), cannot penetrate into the micelle core. POPC glycerol (GL) moieties are located right below the interface at which the RDDs of POPC tails and water intersect. At the surface, the carboxylate groups (OCO-) of CHOAs protrude farther towards the aqueous environment compared to the PO4- and NC3+ groups of POPCs. Speaking of the positioning of CHOAs, the RDD peaks of sterol body beads are located almost at the same distance from the micelle com, however the methyl groups

(embodied in R1 and R3 (not shown on the figure to maintain visual clarity) can penetrate slightly deeper. This indicates that CHOA sterol bodies are mostly aligned more or less parallel at the surface with their hydrophilic faces exposed to the aqueous environment. However, the broadness of the distributions also suggest that they can also adopt more perpendicular orientations with the ROH end group penetrating deeper towards the core. The significantly farther localization of the OCO beads from the surface (indication of a tilt towards water) is a result of the rigid structure of CHOAs giving them the typical wedge-like shape. Finally, there is an ionic double layer around the micelle surface, of which the first and second shells are comprised of Na+ and Cl- ions, respectively. These structural features are very similar to those of plain mixed micelles obtained at fed state conditions, which have been reported elsewhere (Tuncer and Bayramoglu, 2019).

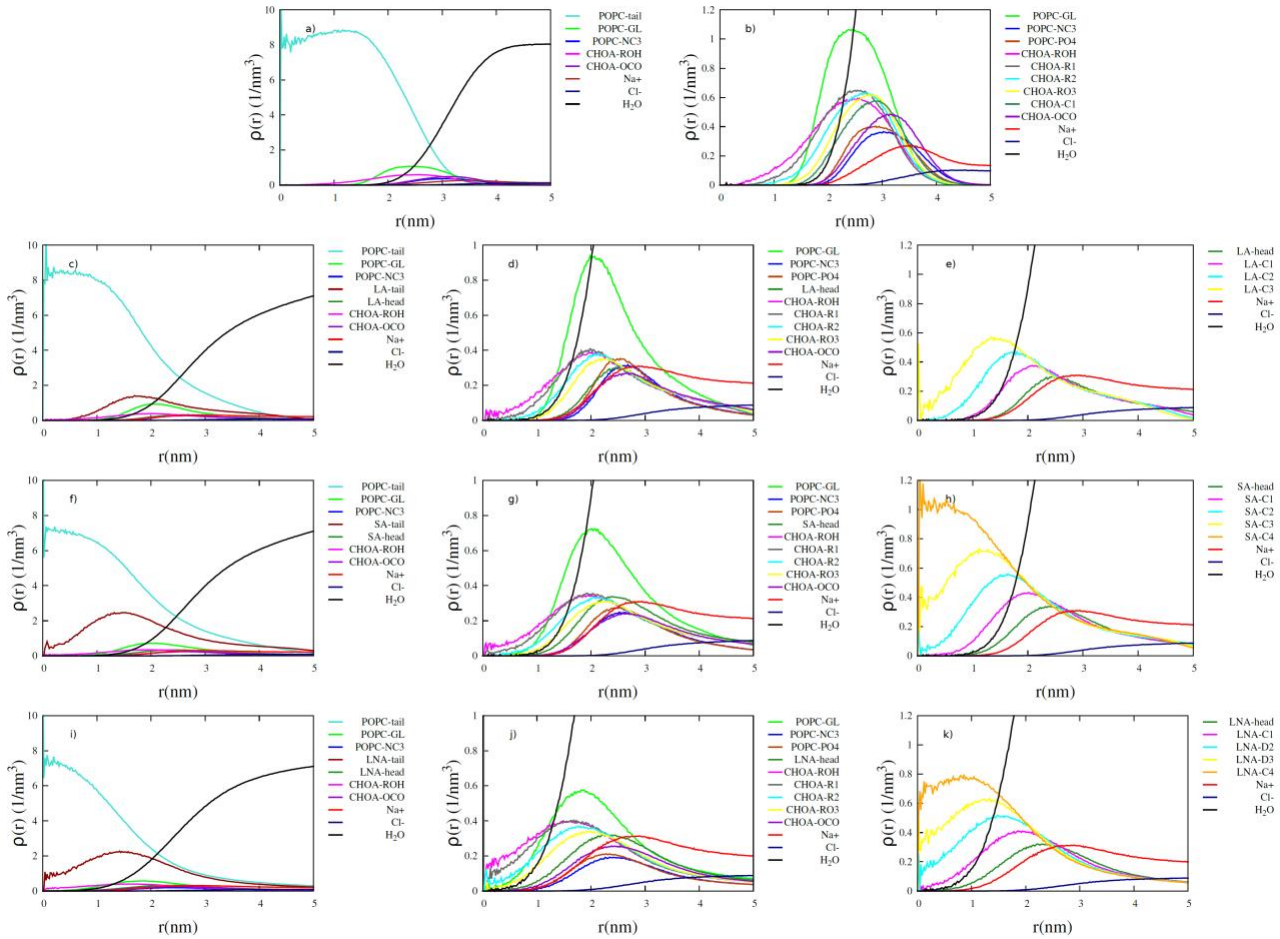

Figure 4. Radial density distributions (ρ(r)) of different moieties of the constituent molecules, water and ions with respect to the micelle com for the representative (a-b) Plain, (c-e) LA, (f-h) SA, and (i-k) LNA mixed micelles.

Type I and type II angle calculations (Fig.5) give further information about the internal and surface orientations and conformations of the constituent molecules. Here, Type I refers to the angle between a vector formed by two selected beads on a molecule and the radial vector (calculated as the vector from the com of the micelle to the midpoint of the selected beads' positions), and Type II refers to the angle between two vectors in a molecule denoted by 3 beads in total, of which the middle bead is the origin of both vectors and the remaining ones indicate their directions (Tuncer and Bayramoglu, 2019). Firstly, type I angle between the RO3-ROH vector on the sterol body and the micelle radial vector with the highest probability was around 100˚ (Fig.5a) verifying that sterol bodies most likely adopt almost flat alignments on the surface. The broadness of the distribution implies the possibility of a wider range of orientations, however. The most probable internal angle (OCO-C1-ROH, type II) observed in CHOAs was found as ~135˚ (Fig.5e) confirming the predictions of RDDs indicating a wedge-like shape for the molecule. Regarding the alignment of POPC head groups on the surface, the most probable type I angle between the PO4-NC3 vector and the radial axis was 75˚ (Fig.5b), indicating a close-to-parallel orientation. Similarly, possible miscellaneous alignments are suggested by the broadness of the distribution. Fig.5c shows the orientations of the upper (D3B-C1B) and lower (C5B-D3B) parts of the POPC oleoyl tails. D3B-C1B section of the tail makes an angle of 40˚, while C5B-D3B section makes an angle of 60˚ with the radial axis at the highest probability. The broad range of distributions, especially for the lower section, indicates a disordered arrangement of the oleoyl tails in the micelle core. The intrinsic angle of the kick in the tail mostly populated around 125˚ (Fig.5f). The palmitoyl tails of POPCs showed that the most probable angle with the micelle radial vector around 50˚ (Fig.5d). They exhibited more stretched conformations compared to the oleoyl tails

since the type II C1A-C2A-C4A angle populated around 145˚ (Fig.5g). Overall, the POPC tails were shown to exhibit disordered organization within the micelle core giving it a fluid nature, which has also been reported in other similar studies before (Bogusz et al., 2000; Jójárt et al., 2014; Marrink and Mark, 2002; Tuncer and Bayramoglu, 2019; Tunçer and Bayramoğlu, 2022).

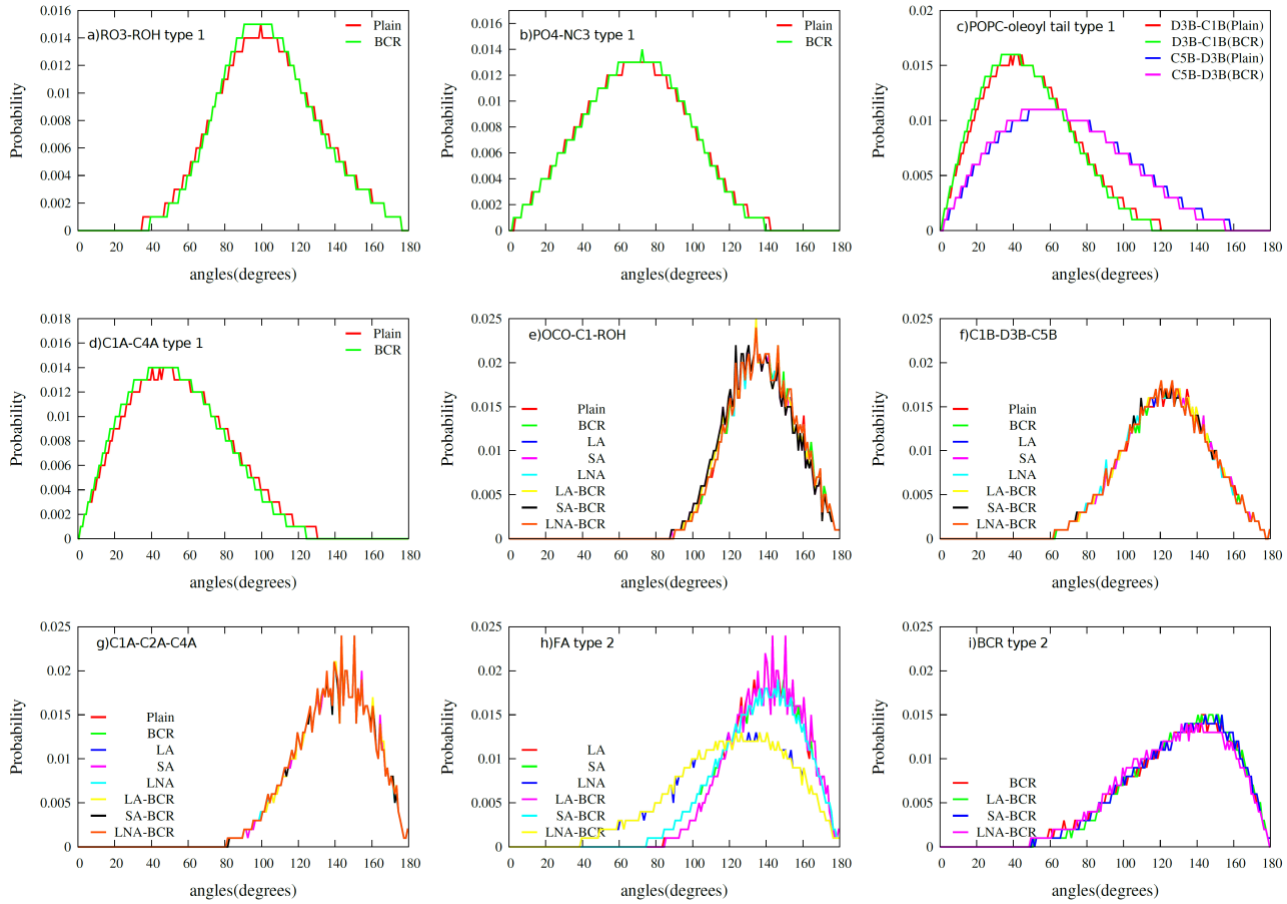

Figure 5. (a-d) Type I angle (between a vector of two selected beads in a molecule and the micelle radial vector) distributions for the representative plain and BCR micelles. The origin of each vector is the first specified bead; hence the direction of each vector is from the first to the second specified bead. The radial vector is the vector that connects the micelle com to the midpoint of the selected beads' positions. (e-i) Type II angle (between two vectors in a molecule) distributions for all representative micelles. The origin of each vector is the middle specified bead; the directions of the vectors are from the middle to the end beads.

Solubilization of Fatty Acids in the Representative Duodenal Cholate-POPC Mixed Micelle

Fig.2(b-d) shows the final frames corresponding to the simulations of the systems named as 'Fa-LA', 'Fa-SA', and 'Fa-LNA', respectively. As expected, the representative plain MM swells and transforms into more elongated shapes with the incorporation of FAs into their structure. The consequent structural changes are discussed in detail below. The final phase behavior of the systems will be addressed firstly. The figure shows that the systems incorporating SA and LNA ended up in a single MM, while two MMs were formed within the system incorporating LA. Of these two MMs, the first one was a smaller MM only composed of LA and CHOA molecules, while the other one was a larger MM composed of all three types of surfactants (LA, POPC, CHOA). As the molecular concentrations were the same in all systems, the situation must be related to the effect of FA chain length and rigidity. LA is a medium-chain saturated FA. It has the shortest and the most rigid tail among the other FAs studied. Moreover, all the FAs are used in fully deprotonated forms, which forces the localization of the charged head groups at the micelle surface, and does not allow the short LA tails to reach the micelle core (Fig.4(c,e)). At the fixed molecular ratios and system sizes used in this study, this situtation seems to limit the extent of elongation of the LA micelle as further elongation would probably result in disproportionate regions in the core in terms of packing density (low density micelle coms populated only by end groups of POPC tails, followed by higher density region populated by both POPC and LA tails), which would presumably decrease the micelle stability. A similar behavior was not observed in 'Fa-SA' and 'Fa-LNA' systems probably because the SA and LNA tails were long enough to reach the micelle core (Fig.4(h,k)), hence the elongation of the micelles were not limited.

The time dependent number of free CHOAs and N_w calculations (not shown) performed over 10 μs trajectories showed that the simulations for the systems 'Fa-LA', 'Fa-SA' and 'Fa-LNA' converged after 2.5, 3 and 3.5 μs. Therefore, the cumulative probability distribution of micelle aggregation number analyses was made over the last 6-7 μs of the production runs (Fig.3(b-e)). Although

the cumulative probability of the MM composed of only LA and CHOA was found to be the highest in the 'Fa-LA' system (Fig.3b), the other micelle with 225 members composed of POPC, LA and CHOA (Fig.3c) was chosen for further analyses concerning the importance of micelle size in solubilization of β-carotene. For the 'Fa-SA' and 'Fa-LNA' systems, the most stable MMs were found to have 269 and 272 members, respectively. The compositional details and the structural properties of these MMs are given in Table 2. The results indicate that the increase in micelle size with incorporation of FAs is correlated with the FA chain length and unsaturation, which supports the findings of others (El Aoud et al., 2021; Gleize et al., 2013; Kossena et al., 2003; Phan et al., 2015; Yuan et al., 2018). The radii of gyration of the representative LA, SA and LNA MMs were calculated as 3.264, 3.685, and 4.425 nm, respectively, exhibiting an increasing trend with FA tail length and unsaturation. The corresponding principal moments of inertia ratios indicate that all types of FAs caused an elongation in the plain MM, the extent of which is also in the same direction of increasing chain length and unsaturation. LA and SA micelles ended up as elongated ellipsoids in shape, while LNA micelle was in the form of a flexible (worm-like) cylinder. The transformation from a spheroidal towards a cylindrical shape with the incorporation of FAs can be attributed to the increased micellar lipid/BS ratios, which has been shown experimentally before on plain MMs (Cohen et al., 1998; Hjelm et al., 1992, 1990). It is known that POPC and FA molecules have lower spontaneous curvature compared to that of CHOAs. Therefore, the decrease in the micellar BS ratio leads to formation of morphologies having lower curvatures; i.e., elongated structures (Madenci et al., 2011). Note that the percentage of CHOAs decreased from 57% (plain MM) to ~35% in the micelles with FAs. Comparison of the SA micelle with LNA micelle reveals the effect of FA unsaturation on the morphology. Although LNA micelle differs from SA micelle by only 3 CHOAs, the variations in the size and shape of both MMs are drastic. LNA tails occupy a significantly larger steric volume due to their ability to fold over themselves owing to the two inherent double bonds (embodied in D2 and D3 beads). This is evident both from FA length and type II intrinsic angle calculations. Although the chain length of SA and LNA are identical, the average FA lengths (calculated as the average distance between the COO and last tail bead in a FA) in the corresponding micelles were determined as 1.556 nm and 1.335 nm, respectively, indicating that LNA tails mostly adopted rather folded conformations. This is also supported by the type II angle calculations (Fig.5h), which reveals that LNA tails were able to sample a wider range of conformations (including ones giving an intrinsic angle as low as 40˚) compared to both LA and SA. This, in turn, seem to have resulted in a much more fluid micelle core as evidenced by the thinner, longer and more flexible structure of the LNA micelle.

RDDs of the selected moieties of the constituent molecules with respect to the micelle coms are given Fig.4(c-k). To begin with, note that the RDDs of MMs incorporating FAs are broader and right-skewed compared to that of the plain MM, which is obviously due to the evolution of micelle shapes from spheroidal to ellipsoidal/cylindrical. In general, the arrangement of ions/waters around the micelles and the internal organization of molecular groups show similar features in all micelles including the plain MM. The micelle surfaces are populated with the charged head groups of POPC and FAs as well as CHOAs, which are surrounded by an electrical double layer comprised of Na+ and Cl- ions. Incorporation of FAs led to sharing of micelle cores between POPC and FA tails, which seems to have increased the core packing densities compared to the plain MM (as suggested by the disappearance of the region of diminishing probability (0-1 nm) in the POPC tail RDDs, which was observed in the plain MM (Fig.4a) indicating lower core density). The RDD peaks corresponding to the FA tail beads being sequentially aligned in all micelles suggests that the tails were oriented more or less pointing towards the center. However, visual inspection verified that this alignment was not perfect. It is inferred that the packing frustrations in the core caused pushing of POPC tails more towards the micelle center even in the case of LA micelle in which the shorter LA tails were not able to reach the center (Fig.4(c, e)). The effects of FA chain length and unsaturation on the micelle shape and fluidity are also reflected on the corresponding RDDs. First of all, the long-chain SA and LNA tails were able to reach the micelle centers as opposed to LA tails. The probability of SA tails occupying the micelle center was higher owing to its much more rigid structure compared to LNA. Furthermore, the probability of CHOA end groups (especially ROH and R1 beads) to sample micelle cores have increased due to the elongation in micelles, which is more evident in the SA and LNA micelles compared to LA. This effect was the most significant in the longer, thinner and more flexible LNA micelle owing to its apparently higher fluidity. Because of the same reason, water molecules were able to penetrate towards the micelle center to a larger extent as well.

As the MMs incorporating FAs were far from being spheroidal, type I angle calculations would give misleading results. Therefore, only the outcomes of type II angle calculations are given in Fig.5(e-h). The results indicate that the conformations of CHOAs and POPC tails do not change with respect to the presence or type of FAs. It is only the FAs which show conformational differences in the micelles. The most probable intrinsic angle within LA and SA molecules in the corresponding MMs were determined as 140˚, while it was 120˚ for LNA due to its ability to fold over itself. However, the broadness of the distributions is different in each MM; i.e., there is an increasing trend with FA chain length and unsaturation.

Solubilization of β-carotene in the Mixed Micelles

The convergence of the simulations for the systems 'Fa-BCR', 'Fa-LA-BCR', 'Fa-SA-BCR' and 'Fa-LNA-BCR' was pretty fast (within ~400 ns) as the initial configurations comprised of 3 BCR molecules randomly distributed around already equilibrated MMs (extracted from the previous simulations mentioned above). Therefore, the cumulative probability distribution of micelle aggregation number analyses was made over the entire trajectories (Fig.3(f-i)). For the 'Fa-BCR', 'Fa-LA-BCR', 'Fa-SA-BCR' and 'Fa-LNA-BCR' systems, the most stable MMs were found to have 155, 226, 271, and 275 members, respectively. Fig.2(e-h) shows the corresponding final frames. The compositional details and

the structural properties of these MMs are given in Table 2.

It is known that duodenal MMs must be large enough to effectively solubilize bioactive molecules as large as BCRs. It is speculated that MMs swell with the incorporation of BCRs into their structure. Therefore, it was interesting to observe that solubilization of 3 BCRs in the representative plain MM did not lead to an increase in the micelle size (whereas it did in SA-and LNA MMs) despite the fact that it was the smallest among all of them. No significant changes in the R_g and the total SASA were observed with the incorporation of BCRs, while there was a very small increase in the I_1/I_2 and I_2/I_3 ratios indicating a slight transformation towards a more spheroidal shape. Furthermore, the length of the POPC-oleoyl and palmitoyl tails did not change with the incorporation of BCRs, and no additional CHOA molecules were needed to adsorb on the micelle surface to maintain its stability. All these findings suggest the following; i. the initial size of the representative plain MM was large enough to accommodate 3 BCR molecules, ii. the core density of the MM was low enough to allow the solubilization of 3 BCRs without causing any swelling or instability, iii. the hydrophobic core packing density increased with the incorporation of the BCRs. The latter effect seems to be similar to the condensation of POPC lipid membranes induced by carotenoids (Mostofian et al., 2020). These results, however, are in opposition to those found for a smaller representative fed state MM in another study of our group (not published, in preparation). Therefore, it can be said that if the initial micelle size is not high enough to accommodate the BCRs, the micelle swells (with a concomitant decrease in hydrophobic core density resulting from sweeping away of the POPC tails), however, if the micelle is large enough, whether or not swelling will take place depends on the hydrophobic core density. For the case that the core density before the incorporation of BCRs is already high, micelle swelling is expected (as in the case with SA-BCR and LNA-BCR micelles-discussed below). The increase in the core packing density of the plain MM upon solubilization of BCRs, which is similar to what was observed with the joining of FAs (see the previous section), is demonstrated by the corresponding RDDs (Fig.6(a-c)). It is observed that the BCRs occupy the core with especially their middle groups localized at the micelle com. This seems to have resulted in a somewhat sweeping away of the POPC tails from the center, while pushing the RDD peaks of POPC GL and head groups slightly towards the surface (Fig.6b). Note that the RDD peak positions of CHOA beads did not change, and the POPC tail lengths and the type II intrinsic angle distributions (Fig.5(f, g)) were unaltered as well as the micelle size. Therefore, the closer positioning of POPC head groups with CHOAs on the surface was possible either due to a slight increase in surface packing density or transformation towards a slightly more spherical shape. On the other hand, the trend in the alignment of the tails with the micelle radial vector increased slightly as indicated by the small left-shifts of the corresponding type I angle distributions (Fig.5(c, d)). Hence, it can be stated that the increased packing density in the core leads to slightly improved alignment (ordering) of POPC tails with the radial direction. The reason that this effect was not observed more apparently from the plots is probably due to the use of a CG model in the representation of the molecules. A similar ordering effect of β-carotene on POPC tails in lipid membranes has been reported before (Jemioła-Rzemińska et al., 2005). The RDDs also give idea about the interactions of BCRs with the other constituent molecules. As expectedly, they are mainly in interaction with POPC tails in the core. However, they also have some sort of interaction with the CHOAs, especially with the end ROH groups. The interactions of BCR head groups with ROH beads of CHOAs are more prominent compared to those of the middle beads, obviously due to the preferred localization of the mid-groups at the micelle com (Fig.6c). Finally, note that BCRs most probably adopted a slightly bent conformation (with an intrinsic angle of ~140˚, Fig.5i) within the plain MM. However, the broad distribution suggests that they were occasionally able to sample more bent conformations as well. Visual inspection showed that this was possible due to the individual BCRs' wrapping around themselves in the micelle core (Fig.2i). The exemplary snapshot given in the figure also gives idea about the interactions between individual BCRs. It is observed that BCRs can interact with each other through both the middle and head groups, however the main contribution to the clustering of 3 BCRs seems to be the hydrophobic interactions between the head groups. This is not surprising since 3 methyl groups are embodied in each head group, while a single CH_3 is embodied in each middle interaction site of a BCR.

The solubilization of BCRs in the MMs incorporating FAs also resulted in some morphological changes, which depends on the type of FA. The most interesting finding was that the size of the LA micelle decreased to 3.102 nm with the incorporation of BCRs. The small reduction in size was accompanied by a slight shape transformation; i.e., LA-BCR micelle exhibited a somewhat more spheroidal form compared to the LA micelle. On the other hand, a drastic increase in micelle size with a significant shape transformation was observed in the SA micelle with the solubilization of BCRs. The substantial increase in R_g (4.395 nm) was clearly a result of the evolution from an elliptical to a cylindrical form. The worm-like LNA micelle, however, did not show any significant size or shape transformations upon the incorporation of BCRs. All these variations in the response of MMs to solubilization of BCRs can be explained on the grounds of differences in micelle core densities and fluidity, which have been shown to be a function of FA chain length and unsaturation above. First of all, the size reduction observed in the LA micelle upon the addition of BCRs (despite the fact that it was the smallest amongst the other FA incorporating MMs) can be rationalized by the non-existence of short LA tails in the micelle com (Fig.3e) having resulted in a lower density central region. By this means, BCRs were able to solubilize within the core in a moderate competition with the POPC tails. The interactions between the BCRs and POPC tails in the core must have caused a condensation effect similar to the case observed with the plain MM, as explained above. The same effect was not observed in the SA and LNA micelles most probably because the micelle coms were already densely packed by POPC and FA tails, and these MMs were thinner and longer in shape. Therefore, incorporation of BCRs must have caused a significant competition for

the core between BCRs and POPC/FA tails. The competition was expectedly strongest in the SA-BCR micelle due to the long and rigid tails of SA, which could only be alleviated by the elongation of the micelle. The fact that a significant elongation was not observed with the LNA-BCR micelle can be attributed to the already flexible and fluid nature of the LNA micelle (see the previous section), which readily allowed the solubilization of 3 BCRs within its core.

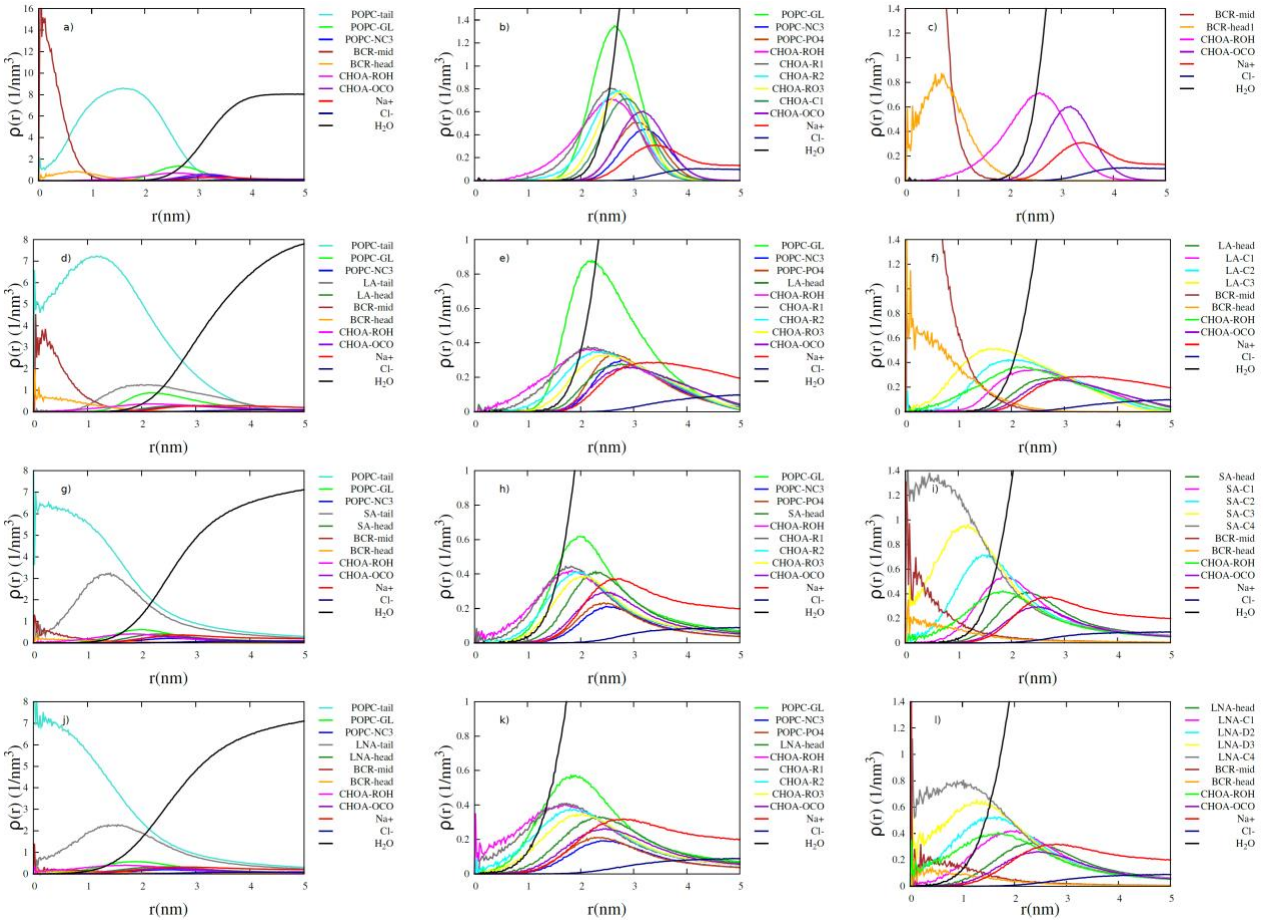

Figure 6. Radial density distributions (ρ(r)) of different moieties of the constituent molecules, water and ions with respect to the micelle com for the (a-c) LA-BCR, (d-f) SA-BCR, and (g-i) LNA-BCR mixed micelles.

The details of the internal organization of the constituent molecules in the FA incorporating MMs are shown in Fig.6(d-l). In all MMs, BCRs are positioned at the hydrophobic core with their middle-groups preferably localized in the micelle com. However, this preference levels off in the SA-BCR and LNA-BCR MMs owing to the effects of micelle shape and fluidity. In the ellipsoidal LA-BCR micelle, solubilization of BCRs swept some POPC tails away from the com (Fig.6d), while they pushed LA tails slightly towards the surface as indicated by the small right-shifts in the peaks of the corresponding RDDs (Fig.6f). The distributions show that BCRs mainly interact with the POPC tails in the core whereas they have partial interaction with especially the end beads of CHOAs and LA tails. On the other hand, they seem to be in full interaction with POPC and FA tails in the other MMs due to the differences in the micelle forms, while they partially interact with the end groups of CHOAs (Fig.6(g-l)). The effect of FA unsaturation also manifests itself on the extents of distributions, especially on those of CHOAs, FAs and water. Note that all of these molecules can penetrate to a larger extent towards the core in the LNA-BCR micelle because of its high fluidity induced by flexible LNA tails. The superior flexibility of the tails is evidenced by the intrinsic type II angle calculations (Fig.5h). Another consequence of the more fluid structure of the LNA-BCR micelle was that BCRs were able to move more freely within the core compared to other MMs. Visual inspection showed that all three BCRs remained together forming a cluster in LA-BCR and SA-BCR MMs, while they had more freedom to move separately within the core of LNA-BCR. This is illustrated in Fig.2(j-l). The BCR length (Table 2) and intrinsic type II angle calculations (Fig.5i) suggest further that the molecules were also able to sample slightly more bent conformations within this MM. Therefore, it is inferred that the movements of BCRs in the core are restricted by the rigidity of the tails of saturated LA and SA. On the other hand, the significantly higher fluidity of the LNA-BCR micelle seems to allow BCRs both to adopt slightly more bent conformations and travel more freely inside the core.

Conclusion

In this study, it was aimed to investigate the morphological changes in a representative fasted state duodenal MM upon the incorporation of FAs with different characteristics and the structural changes observed in these micelles taking place upon the solubilization of BCRs by means of CG MD simulations. The effects of FA chain length and unsaturation on the structural properties were investigated through the use of

medium-chain saturated LA, long-chain saturated SA and long-chain polyunsaturated LNA. To the best of our knowledge, this is the first study that demonstrates the accompanying structural transformations in MMs with solubilization of BCRs and reveals a detailed picture of the internal morphology.

A representative fasted state plain MM composed of CHOA and POPC was obtained with the desired size and shape in the first place. The core-shell ellipsoidal model proposed for the interior morphology was confirmed with simulations. Later, the solubilization of FAs within this MM was examined. It was shown that the plain MM swelled and transformed into more elongated forms with the incorporation of FAs. The increase in size was in line with increasing FA chain length and unsaturation. The systems incorporating SA and LNA ended up in a single MM, while two MMs were formed within the system incorporating LA. The difference in the behavior of LA system was attributed to the effect of FA chain length combined with the use of fully deprotonated FAs. The latter forces the charged head groups of LAs to be located at the micelle surface, which limits the extension of short LA tails as far as to the micelle center of mass. It seems to be a reasonable assumption that this situation limits the growth of the MMs as it would result in regions with varying packing densities in the core leading to instability. The fact that micelle growth was not limited in systems with long-chain SA and LNA supports this assumption. The effect of FA unsaturation also manifested itself on the micelle morphology. A much more fluid micelle core was obtained as evidenced by the thinner, longer and more flexible structure of the LNA MM. It was expected that solubilization of 3 BCRs within all the MMs would lead to micelle swelling. However, swelling was observed only in the MMs with long-chain SA and LNA, but not in LA MM despite its smaller size. The results indicate provided that the micelle is initially large enough to accommodate the BCRs, whether or not swelling will take place depends on the hydrophobic core density. For the case that the core packing density of molecules before the incorporation of BCRs is already high, micelle swelling is expected. Otherwise, even a slight shrinkage in size (due to an effect similar to the condensation of lipid bilayers induced by carotenoids) may occur, which was the case observed when BCRs were solubilized in the plain and LA MMs. The increase in micelle size was very small in LNA-BCR compared to the drastic change observed in SA-BCR accompanying elliptical-to-cylindrical shape transformation. This was due to the fluid nature of the worm-like LNA micelle, which readily allowed the solubilization of 3 BCRs within its core. Another consequence was that BCRs were able to move more freely within the core compared to other MMs. In contrast, the movements of BCRs were restricted by the rigidity of the tails of saturated LA and SA in the corresponding MMs.

Overall, by resolving the internal structures of representative fasted state MMs incorporating BCRs, this study gives valuable insight into the effects of FA chain length and unsaturation on the solubilization behavior of dietary MMs. However, it should be noted that simulations at a fixed lipid concentration, molecular ratio or pH do not provide a holistic view of the micellarization of BCR in duodenum. More systematic future studies elucidating the effects of many other factors are needed to complement the knowledge. Nevertheless, the information gained in this work is expected to give direction to the development of design strategies for effective BCR delivery systems.

Compliance with Ethical Standards

Conflict of interest

The authors declared that for this research article, they have no actual, potential or perceived conflict of interest.

Author contribution

The contribution of the authors to the present study is equal.

All the authors read and approved the final manuscript. All the authors verify that the Text, Figures, and Tables are original and that they have not been published before.

Ethical approval

Ethics committee approval is not required.

Funding

This study was supported by The Scientific and Technological Research Council of Turkey (TUBITAK) (grant number:118O378). Computing sources were provided by the National Center for High Performance Computing of Turkey (UHEM) under grant number 5004012016.

Data availability

Not applicable.

Consent for publication

Not applicable.

References

Abraham, M.J., Murtola, T., Schulz, R., Páll, S., Smith, J.C., Hess, B., Lindah, E. (2015). Gromacs: High performance molecular simulations through multi-level parallelism from laptops to supercomputers. SoftwareX 1–2, 19–25. https://doi.org/10.1016/j.softx.2015.06.001

Berendsen, H.J.C., Postma, J.P.M., Gunsteren, W.F. Van, Dinola, A., Haak, J.R. (1984). Molecular dynamics with coupling to an external bath. J. Chem. Phys. 3684. https://doi.org/10.1063/1.448118

Birru, W.A., Warren, D.B., Ibrahim, A., Williams, H.D., Benameur, H., Porter, C.J.H., Chalmers, D.K., Pouton, C.W. (2014). Digestion of phospholipids after secretion of bile into the duodenum changes the phase behavior of bile components. Mol. Pharm. 11, 2825–2834. https://doi.org/10.1021/mp500193g

Bogusz, S., Venable, R.M., Pastor, R.W. (2000). Molecular Dynamics Simulations of Octyl Glucoside Micelles:

Structural Properties. J. Phys. Chem. B 104, 5462–5470. https://doi.org/10.1021/jp000159y
Bustos, A.Y., Raya, R., de Valdez, G.F., Taranto, M.P. (2011). Efflux of bile acids in Lactobacillus reuteri is mediated by ATP. Biotechnol. Lett. 33, 2265–2269. https://doi.org/10.1007/s10529-011-0696-3
Cheng, X., Jo, S., Lee, H.S., Klauda, J.B., Im, W. (2013). CHARMM-GUI micelle builder for pure/mixed micelle and protein/micelle complex systems. J. Chem. Inf. Model. https://doi.org/10.1021/ci4002684
Clulow, A.J., Parrow, A., Hawley, A., Khan, J., Pham, A.C., Larsson, P., Bergström, C.A.S., Boyd, B.J. (2017). Characterization of Solubilizing Nanoaggregates Present in Different Versions of Simulated Intestinal Fluid. J. Phys. Chem. B 121, 10869–10881. https://doi.org/10.1021/acs.jpcb.7b08622
Cohen, D.E., Thurston, G.M., Chamberlin, R.A., Benedek, G.B., Carey, M.C. (1998). Laser light scattering evidence for a common wormlike growth structure of mixed micelles in bile salt- and straight-chain detergent-phosphatidylcholine aqueous systems: Relevance to the micellar structure of bile. Biochemistry 37, 14798–14814. https://doi.org/10.1021/bi980182y
de Jong, D.H., Liguori, N., van den Berg, T., Arnarez, C., Periole, X., Marrink, S.J. (2015). Atomistic and Coarse Grain Topologies for the Cofactors Associated with the Photosystem II Core Complex. J. Phys. Chem. B 119, 7791–7803. https://doi.org/10.1021/acs.jpcb.5b00809
El Aoud, A., Reboul, E., Dupont, A., Mériadec, C., Artzner, F., Marze, S. (2021). In vitro solubilization of fat-soluble vitamins in structurally defined mixed intestinal assemblies. J. Colloid Interface Sci. 589, 229–241. https://doi.org/10.1016/j.jcis.2021.01.002
Fatouros, D.G., Bergenstahl, B., Mullertz, A. (2007). Morphological observations on a lipid-based drug delivery system during in vitro digestion. Eur. J. Pharm. Sci. 31, 85–94. https://doi.org/10.1016/j.ejps.2007.02.009
Fatouros, D.G., Walrand, I., Bergenstahl, B., Mullertz, A. (2009). Physicochemical characterization of simulated intestinal fed-state fluids containing lyso-phosphatidylcholine and cholesterol. Dissolution Technol. 16, 47–50. https://doi.org/10.14227/DT160309P47
Gleize, B., Tourniaire, F., Depezay, L., Bott, R., Nowicki, M., Albino, L., Lairon, D., Kesse-Guyot, E., Galan, P., Hercberg, S., Borel, P. (2013). Effect of type of TAG fatty acids on lutein and zeaxanthin bioavailability. Br. J. Nutr. 110, 1–10. https://doi.org/10.1017/S0007114512004813
Hess, B., Bekker, H., Berendsen, H.J.C., Fraaije, J.G.E.M. (1997). LINCS: A linear constraint solver for molecular simulations. J. Comput. Chem. 18, 1463–1472. https://doi.org/10.1002/(SICI)1096-987X(199709)18:12<1463::AID-JCC4>3.0.CO;2-H
Hjelm, R.P., Alkan, M.H., Thiyagarajan, P. (1990). Small-Angle Neutron Scattering Studies of Mixed Bile Salt-Lecithin Colloids. Mol. Cryst. Liq. Cryst. Inc. Nonlinear Opt. 180, 155–164. https://doi.org/10.1080/00268949008025796
Hjelm, R.P., Thiyagarajan, P., Önyüksel, H. (1992). Organization of phosphatidylcholine and bile salt in rodlike mixed micelles. J. Phyical Chem. 96, 8653–8661. https://doi.org/10.1021/j100200a080
Humphrey, W., Dalke, A., Schulten, K. (1996). VMD: Visual molecular dynamics. J. Mol. Graph. 14, 33–38. https://doi.org/10.1016/0263-7855(96)00018-5
Huo, T., Ferruzzi, M.G., Schwartz, S.J., Failla, M.L. (2007). Impact of fatty acyl composition and quantity of triglycerides on bioaccessibility of dietary carotenoids. J. Agric. Food Chem. 55, 8950–8957. https://doi.org/10.1021/jf071687a
Jemioła-Rzemińska, M., Pasenkiewicz-Gierula, M., Strzałka, K. (2005). The behaviour of β-carotene in the phosphatidylcholine bilayer as revealed by a molecular simulation study. Chem. Phys. Lipids 135, 27–37. https://doi.org/10.1016/j.chemphyslip.2005.01.006
Jójárt, B., Poša, M., Fiser, B., Szori, M., Farkaš, Z., Viskolcz, B. (2014). Mixed micelles of sodium cholate and sodium dodecylsulphate 1:1 binary mixture at different temperatures - Experimental and theoretical investigations. PLoS One 9, 1–9. https://doi.org/10.1371/journal.pone.0102114
Khoshakhlagh, P., Johnson, R., Nawroth, T., Langguth, P., Schmueser, L., Hellmann, N., Decker, H., Szekely, N.K. (2014). Nanoparticle structure development in the gastro-intestinal model fluid FaSSIF mod6.5 from several phospholipids at various water content relevant for oral drug administration. Eur. J. Lipid Sci. Technol. 116, 1155–1166. https://doi.org/10.1002/ejlt.201400066
Kossena, G.A., Boyd, B.J., Porter, C.J.H., Charman, W.N. (2003). Separation and characterization of the colloidal phases produced on digestion of common formulation lipids and assessment of their impact on the apparent solubility of selected poorly water-soluble drugs. J. Pharm. Sci. 92, 634–648. https://doi.org/10.1002/jps.10329
Madenci, D., Salonen, A., Schurtenberger, P., Pedersen, J.S., Egelhaaf, S.U. (2011). Simple model for the growth behaviour of mixed lecithin-bile salt micelles. Phys. Chem. Chem. Phys. 13, 3171–3178. https://doi.org/10.1039/c0cp01700k
Marrink, S. J. (2004). Molecular dynamics simulation of cholesterol nucleation in mixed micelles modelling human bile. In G. Adler, M. Fuchs, HE. Blum, & EF. Stange (Eds.), GALLSTONES: PATHOGENESIS AND TREATMENT (pp. 98-105 - 13). (FALK SYMPOSIUM; Vol. 139). Kluwer Academic Publishers.
Marrink, S.J., Mark, A.E. (2002). Molecular Dynamics Simulations of Mixed Micelles Modeling Human Bile. Biochemistry 41, 17, 5375–5382. https://doi.org/10.1021/bi015613i
Marrink, S.J., Risselada, H.J., Yefimov, S., Tieleman, D.P., De Vries, A.H. (2007). The MARTINI force field: Coarse grained model for biomolecular simulations. J. Phys. Chem. B 111, 7812–7824. https://doi.org/10.1021/jp071097f
Marrink, S.J., Tieleman, D.P. (2013). Perspective on the Martini model. Chem. Soc. Rev. 42, 6801. https://doi.org/10.1039/c3cs60093a
Martini General Purpose Coarse-Grained Force Field (2022, August 10). Force field parameters. Retrieved from http://cgmartini.nl/index.php/force-field-parameters

Mashurabad, P.C., Palika, R., Jyrwa, Y.W., Bhaskarachary, K., Pullakhandam, R. (2017). Dietary fat composition, food matrix and relative polarity modulate the micellarization and intestinal uptake of carotenoids from vegetables and fruits. J. Food Sci. Technol. 54, 333–341. https://doi.org/10.1007/s13197-016-2466-7

Matsuoka, K., Maeda, M., Moroi, Y. (2004). Characteristics of conjugate bile salt–phosphatidylcholine–cholesterol–water systems. Colloids Surfaces B Biointerfaces 33, 101–109. https://doi.org/10.1016/j.colsurfb.2003.09.002

Mazer, N.A., Benedek, G.B., Carey, M.C. (1980). Quasielastic Light-Scattering Studies of Aqueous Biliary Lipid Systems. Mixed Micelle Formation in Bile Salt-Lecithin Solutions. Biochemistry 19, 601–615. https://doi.org/10.1021/bi00545a001

Mostofian, B., Johnson, Q.R., Smith, J.C., Cheng, X. (2020). Carotenoids promote lateral packing and condensation of lipid membranes. Phys. Chem. Chem. Phys. 22, 12281–12293. https://doi.org/10.1039/D0CP01031F

Nagao, A., Kotake-Nara, E., Hase, M. (2013). Effects of fats and oils on the bioaccessibility of carotenoids and vitamin E in vegetables. Biosci. Biotechnol. Biochem. 77, 1055–60. https://doi.org/10.1271/bbb.130025

Parrow, A., Larsson, P., Augustijns, P., Bergström, C.A.S. (2020). Molecular Dynamics Simulations on Interindividual Variability of Intestinal Fluids: Impact on Drug Solubilization. Mol. Pharm. 17, 3837–3844. https://doi.org/10.1021/acs.molpharmaceut.0c00588

Phan, S., Salentinig, S., Gilbert, E., Darwish, T.A., Hawley, A., Nixon-Luke, R., Bryant, G., Boyd, B.J. (2015). Disposition and crystallization of saturated fatty acid in mixed micelles of relevance to lipid digestion. J. Colloid Interface Sci. 449, 160–166. https://doi.org/10.1016/j.jcis.2014.11.026

Qian, C., Decker, E.A., Xiao, H., McClements, D.J. (2012). Nanoemulsion delivery systems: Influence of carrier oil on β-carotene bioaccessibility. Food Chem. 135, 1440–1447. https://doi.org/10.1016/j.foodchem.2012.06.047

Sayyed-Ahmad, A., Lichtenberger, L.M., Gorfe, A.A. (2010). Structure and dynamics of cholic acid and dodecylphosphocholine-cholic acid aggregates. Langmuir 26, 13407–13414. https://doi.org/10.1021/la102106t

Schurtenberger, P., Mazer, N., Känzig, W. (1985). Micelle to vesicle transition in aqueous solutions of bile salt and lecithin. J. Phys. Chem. 89, 1042–1049. https://doi.org/10.1021/j100252a031

Suys, E.J.A., Warren, D.B., Porter, C.J.H., Benameur, H., Pouton, C.W., Chalmers, D.K. (2017). Computational Models of the Intestinal Environment. 3. the Impact of Cholesterol Content and pH on Mixed Micelle Colloids. Mol. Pharm. 14, 3684–3697. https://doi.org/10.1021/acs.molpharmaceut.7b00446

Tande, B.M., Wagner, N.J., Mackay, M.E., Hawker, C.J., Jeong, M. (2001). Viscosimetric, hydrodynamic, and conformational properties of dendrimers and dendrons. Macromolecules 34, 8580–8585. https://doi.org/10.1021/ma011265g

Tuncer, E., Bayramoglu, B. (2019). Characterization of the self-assembly and size dependent structural properties of dietary mixed micelles by molecular dynamics simulations. Biophys. Chem. 248, 16–27. https://doi.org/10.1016/j.bpc.2019.02.001

Tunçer, E., Bayramoğlu, B. (2022). Molecular dynamics simulations of duodenal self assembly in the presence of different fatty acids. Colloids Surfaces A Physicochem. Eng. Asp. 644. https://doi.org/10.1016/j.colsurfa.2022.128866

Van Der Spoel, D., Lindahl, E., Hess, B., Groenhof, G., Mark, A.E., Berendsen, H.J.C. (2005). GROMACS: Fast, flexible, and free. J. Comput. Chem. 26, 1701–1718. https://doi.org/10.1002/jcc.20291

Wilson, M.D., Rudel, L.L. (1994). Review of cholesterol absorption with emphasis on dietary and biliary cholesterol. J. Lipid Res. 35, 943–955. https://doi.org/10.1016/S0022-2275(20)40109-9

Wright, A.J., Pietrangelo, C., MacNaughton, A. (2008). Influence of simulated upper intestinal parameters on the efficiency of beta carotene micellarisation using an in vitro model of digestion. Food Chem. 107, 1253–1260. https://doi.org/10.1016/j.foodchem.2007.09.063

Yao, K., Mcclements, D.J., Xiao, H., Liu, X. (2019). Improvement of carotenoid bioaccessibility from spinach by co-ingesting with excipient nanoemulsions: impact of the oil phase composition. Food Funct. 10, 5302–5311. https://doi.org/10.1039/c9fo01328h

Yuan, X., Liu, X., Mcclements, D.J., Cao, Y., Xiao, H. (2018). Enhancement of phytochemical bioaccessibility from plant-based foods using excipient emulsions : impact of lipid type on carotenoid solubilization. Food Funct. 9, 4352–4365. https://doi.org/10.1039/c8fo01118d